Catalysis Today 369 (2021) 193–202

Contents lists available at ScienceDirect

Catalysis Today

journal homepage: www.elsevier.com/locate/cattod

Co-catalyst free ethene dimerization over Zr-based metal-organic framework (UiO-67) functionalized with Ni and bipyridine

Mustafa Kømurcu [a], Andrea Lazzarini [a], Gurpreet Kaur [a], Elisa Borfecchia [b], Sigurd Øien-Ødegaard [a], Diego Gianolio [c], Silvia Bordiga [a,b], Karl Petter Lillerud [a], Unni Olsbye [a,*]

[a] Department of Chemistry, University of Oslo, P.O. Box 1033, Oslo, 0315, Norway
[b] University of Turin, Department of Chemistry, Via P. Giuria 7, Turin, 10125, Italy
[c] Diamond Light Source, Harwell Science and Innovation Campus, Chilton, Didcot, OX11 0DE, UK

ARTICLE INFO

Keywords:
Ethene dimerization
Linear alkenes
Ni-MOF
Heterogeneous catalysis
Co-catalyst free

ABSTRACT

Ni functionalized metal organic frameworks (MOF) are promising heterogeneous ethene dimerization catalysts. Activities comparable to or higher than Ni-aluminosilicates have been reported in literature. However, unlike the Ni-aluminosilicates, those Ni-MOFs require a large excess of co-catalyst to initiate the dimerization process and some catalysts generate polymers which lead to catalyst deactivation. Herein, we report a series of Ni(II) and 2,2′-bipyridine-5,5′-dicarboxylate (bpy) functionalized UiO-67 MOF that catalyze the ethene dimerization reaction co-catalyst free. The catalysts were active for ethene dimerization (up to 850 mg butene $g_{cat}^{-1} h^{-1}$) after activation at 300 °C in 10 % O_2 for 360 min and subsequent exposure to flowing ethene (P(ethene) =26 bar, 250 °C) for 240 min. The catalysts yielded up to 6 % conversion with 99 % selectivity to linear 1- and 2-butenes, which formed in non-equilibrated ratios. Overall, the test data indicate that all three linear butenes are formed on a single active site, in accordance with the Cossee-Arlman mechanism. *Ex situ* XAS and CO FT-IR spectroscopy studies point towards Ni monomers or, plausibly, low-nuclearity Ni-multimers, docked at bpy linkers with Ni-Ni distances > 4 Å, as the main active site for the ethene dimerization reaction.

1. Introduction

The industrial transition from naphtha to ethane as feedstock for ethene production has led to a shorter supply of propene and butene conventionally produced from oil [1]. This change has inspired the search for alternative production processes for propene, butene and butadiene, among which ethene oligomerization is a prominent candidate. Dimerization of ethene to linear α-butene is one of a few large-scale homogeneously catalyzed reactions [2]. The reaction is carried out in organic solvents, and a co-catalyst (*e.g.* Et_2AlCl) is required to start the catalytic cycle [3]. With the intention of making the process more practical and sustainable, recent research efforts have focused on the development of heterogeneous dimerization catalysts.

For a long time, Ni-aluminosilicates have been considered the most promising heterogeneous ethene oligomerization catalyst. The important upsides of Ni-aluminosilicate catalysts compared to the traditional homogeneous Ni-complexes is that they do not require a co-catalyst and they may be regenerated by heating in an oxidative atmosphere at elevated temperature to burn off reaction products deposited on the catalyst [4]. Recently, metal-organic framework (MOF) based ethene oligomerization catalysts are appearing [4,5]. Metal–organic frameworks are crystalline, porous materials where the three-dimensional structure consists of metal ions or clusters connected by organic linkers. The synthetic diversity of these materials enables control over density of active sites and pore size, and the ability to incorporate sophisticated chemical functionalities as part of the framework [6,7]. This strategy includes installing homogeneous catalysts onto the organic ligands [8,9], on the metal clusters [10–12] or encapsulating metal particles [13]. The ability to create well-defined active sites on porous solids, opens up the possibility for tailoring MOFs for ethene dimerization reaction.

Notably, Metzger et al. [10] prepared a catalytically active material, Ni-MFU-4 l, by exchanging one of the five Zn^{2+} ions in the MOF cluster with Ni^{2+}. Ni-MFU-4 l achieved the highest activity reported so far for

* Corresponding author.
E-mail address: Unni.olsbye@kjemi.uio.no (U. Olsbye).

https://doi.org/10.1016/j.cattod.2020.03.038
Received 31 October 2019; Received in revised form 8 March 2020; Accepted 17 March 2020
Available online 19 March 2020
0920-5861/© 2020 The Authors. Published by Elsevier B.V. This is an open access article under the CC BY license (http://creativecommons.org/licenses/by/4.0/).

MOF catalysts (TOF = 41500 mol(ethene) mol(Ni)$^{-1}$ h^{-1}) while retaining > 90 % selectivity towards 1-butene. Another method for utilizing the MOF nodes was reported by Madrahimov et al. [11] where nickel grafted 2,2′-bipyridine (bpy) was grafted on the free Zr-OH sites in the NU-1000 cluster. NU-1000-bpy-$NiCl_2$ was shown to be catalytically active with an intrinsic activity for butenes that was an order of magnitude higher compared to the molecular bpy-Ni^{2+} catalyst. In a more recent study, Gonzales et al. [9] utilized the Ni^{2+} functionalized bpy for ethene oligomerization. The bpy linker was reported to be exchanged with the biphenyl linkers of UiO-67 and functionalized with Ni^{2+}. This catalyst was active for ethene oligomerization and products ranging from C_4 – C_{18} was observed. Control experiments showed that Ni^{2+} functionalized UiO-67 was active for ethene oligomerization reaction without the bpy-Ni^{2+} moiety with similar TOF. The authors suggested that the activity originated most likely from excess nickel coordinated to water and hydroxide ligands on the zirconium cluster. Overall, the challenge with product separation and catalyst regeneration, because of polymer formation, persists in most reported Ni-MOF catalysts [9,11,12].

Importantly, most Ni-MOF catalysts published to date are tested as liquid-phase oligomerization catalysts where the use of solvent and co-catalyst, such as diethylaluminum chloride (Et_2AlCl) or methylaluminoxane (MAO), is required in large excess [8–11,14,15]. These compounds are highly flammable, and avoiding their use would have strong impact on process safety. To the best of our knowledge, the only Ni-MOF that has been reported as ethene oligomerization catalyst without a co-catalyst is Ni-CPO-27 [16]. This catalyst was tested using a continuous flow fixed-bed reactor and was active for propene and ethene dimerization at 5 bar and 180 °C. The two major drawbacks of Ni-CPO-27 were the low conversion and the rapid deactivation (conversion < 1 % for propene and 2 % for ethene after 400 min TOS, reaction condition: 5 bar propene, 453 K, WHSV =64 h^{-1}).

The reaction mechanism in Ni-MOFs and Ni-aluminosilicates have been examined both experimentally and computationally in recent publications. Similar to homogeneous catalysts, the Ni-MOFs are generally concluded to operate through the Cossee-Arlman mechanism [8,9,17–19]. Here, the co-catalyst is hypothesized to generate the active metal-alkyl intermediate where oligomerization proceeds by insertion of ethene into a metal-alkyl bond. Since Ni-aluminosilicates do not require a co-catalyst, the active site formation and reaction mechanism have proven difficult to determine and both metallacycle and Cossee-Arlman mechanism have been suggested [20–24]. However, recent experimental and theoretical investigations further support the Cossee-Arlman mechanism. Specifically, Gounder et al. [25] evaluated the ethene dimerization activity of Ni^{2+} sites in Ni-Beta zeolite (0.01–1 kPa, 453 K, WHSV = 0.01–10 h^{-1}) after suppressing contributions from the H^+ sites on the support. Continued formation of 2-butenes on Ni^{2+} -derived active sites, together with ethene assisted formation of $[Ni(II)\text{-}H]^+$ intermediates (based on H_2 co-feed and H/D isotopic scrambling experiments) were found to be consistent with the Cossee-Arlman mechanism. Furthermore, Brogaard et al. performed Density Functional Theory (DFT) calculations of ethene oligomerization in another microporous zeolite-based catalyst, Ni-SSZ-24, and found that the Cossee-Arlman mechanism is energetically favored compared to the metallocycle mechanism in this catalyst. Moreover, the computational results suggested that the ethene oligomerization mechanism is initiated by proton transfer to the zeolite, leading to Ni-H and, furthermore, Ni-alkyl formation as the most abundant intermediate, without the addition of a co-catalyst [20]. Very recently, Brogaard et al. addressed another peculiar observation of ethene oligomerization over microporous Ni-aluminosilicates catalysts, *i.e.*; the second order reaction in P (ethene). DFT-based molecular dynamics simulations were combined with continuous-flow experiments and microkinetic modeling of the same Ni-SSZ-24 zeolite [26]. The authors found that the second order reaction is consistent with a Cossee-Arlman mechanism in which the $(Ni\text{-ethyl-ethene})^+$ complex is solvated in the zeolite pore by the addition of another ethene molecule. Moreover, it was found that such solvatisation dramatically reduces the activation energy of reaction. The excellent C_4 selectivity of the catalyst was ascribed to the entropic penalty of a solvated $(Ni\text{-butyl-ethene}_2)^+$ complex compared to the smaller $(Ni\text{-ethyl-ethene}_2)^+$ complex [25].

The main goal of the current contribution is to elucidate the potential of Ni-MOFs as co-catalyst free, ethene dimerization catalysts that maintain high linear butene selectivity. One of the MOFs that have shown remarkable chemical, thermal and mechanical stability is the UiO-67 belonging to the UiO Zr-MOF series. The UiO-67 framework consist of 12 coordinated $Zr_6(\mu^3\text{-}O)_4(\mu^3\text{-}OH)_4$clusters connected by biphenyl-4,4′-dicarboxylic acid (bpdc) to yield a microporous three-dimensional framework with both tetrahedral and octahedral cavities with diameters of 12 Å and 16 Å, respectively [6] (Fig. 1).

Herein, we report a series of UiO-67 Zr-MOFs where part of the biphenyl linkers was replaced by bipyridine, as grafting sites for Ni ions. Butene yields up to 1850 mg g_{cat}^{-1} h^{-1} were obtained in gas phase without the use of a co-catalyst. Detailed characterization of fresh and used catalyst (SEM-EDS, N_2 adsorption, XRD, TGA, FTIR, XAS) was performed to identify the active site and to verify the structural stability of the catalyst under reaction conditions.

2. Experimental

2.1. Synthesis

UiO-67-bpy was synthesized via a simple one-pot reaction in dimethylformamide (DMF) at 130 °C, using benzoic acid and water as modulators. 135 g of zirconium chloride (1 eq) was added to a 3 L reactor, containing 63 mL distilled water (6 eq) and 2243 mL DMF (50 eq) at room temperature on a stirring plate. This solution was heated and 212 g of benzoic acid (3 eq) was added, and left until completely dissolved. Subsequently, 14 g of [2,2′-bipyridine]-5,5′-dicarboxylic acid (bpy) was added, followed by 126 g of [1,1′-biphenyl]-4,4′-dicarboxylic acid (bpdc). The solution was left at 130 °C, overnight with stirring under reflux. The resulting product was filtered and washed with hot DMF and acetone, followed by drying at 150 °C, overnight. A white powder was obtained which was filtered and washed with hot DMF (three times with 20 mL) and acetone (three times with 20 mL), followed by drying of product at 150 °C, overnight.

The post synthetic metalation of the MOFs was carried out in EtOH with $Ni(acetate)_2{*}4H_2O$ as the metal source. All MOFs were dried at 196 °C in air prior to metalation. The required amount of Ni salt for various Ni:bpy (mol/mol) ratios was dissolved in EtOH (10 mL_{EtOH}/g_{cat}) and mixed with the catalyst in a HDPE bottle. The slurry was sonicated for 30 min, capped and heated overnight at 65 °C. The resulting slurry was washed three times with 10 mL_{EtOH}/g_{cat} and dried in air overnight at 65 °C. The nickel functionalized samples were denoted xNi-UiO-67-bpy_y, where x is the Ni wt % determined by EDS analysis and y stands for the mol % bpy relative to (bpy + bpdc) determined by ^{1}H-NMR.

2.2. Characterization

The bpy content of UiO-67-bpy was determined by liquid-phase ^{1}H-NMR, after digestion of the MOF in a NaOH/ D_2O solution. 20 mg of dry sample was weighed in a centrifuging tube and 1 mL of 1 M NaOH (in D_2O) was added. The tube was shaken properly to obtain a homogeneous suspension and kept overnight for digestion. After centrifuging the digested suspension for 15 min, 600 µL solution was pipetted to an NMR tube. Liquid ^{1}H NMR spectra were obtained with a Bruker AVII 400 NMR Spectrometer (400 MHz). The relaxation delay (d1) was set to 20 s with 64 scans.

Powder X-ray diffraction (PXRD) patterns of the MOF samples before and after metalation and after reaction were obtained using a Bruker D8 Discover diffractometer with Cu K_α radiation (λ = 1.5406 Å).

The textural properties of the samples were derived from N_2

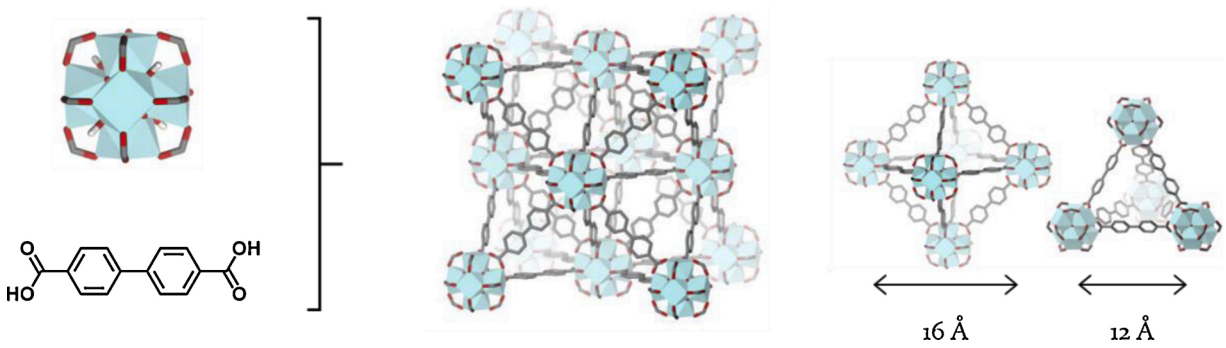

Fig. 1. The $Zr_6(\mu^3\text{-}O)_4(\mu^3\text{-}OH)_4(COO)_{12}$ clusters that are connected by bpdc linkers to form the three-dimensional microporous framework of UiO-67 with tetrahedral and octahedral cages. Atom color: black, C; red, O; blue, Zr. Adopted from [27]. (For interpretation of the references to colour in this figure legend, the reader is referred to the web version of this article).

adsorption isotherms, measured at −196 °C, using a BELSORP-mini II instrument. Unless specified otherwise, all samples were outgassed in vacuum for 1 h at 80 °C and 3 h at 300 °C, and then measured. The catalyst pore volumes and surface areas were determined using the t-plot and BET methods.

The elemental composition, specifically Ni/Zr ratio, was determined by energy-dispersive X-ray (EDS) spectroscopy at 10 kV accelerating voltage utilizing a X-flash 6|10 detector. The stability of the catalysts in synthetic air, as well as the amount of retained hydrocarbons after reaction was determined by thermogravimetric analysis (TGA) on a Netzsch STA 449 F3-Jupiter instrument. Approximately 20 mg of catalyst was heated under a flow of synthetic air (25 mL/min) to 800 °C at a rate of 5 °C/min.

FT-IR measurements with CO probing at 77 K were performed in transmission mode using a Vertex80 spectrometer from Bruker, equipped with a liquid nitrogen cooled MCT detector. Each spectrum was obtained averaging 64 scans with a resolution of 2 cm^{-1}. The pure sample in powder form was pressed into a thin self-sustained pellet and placed in a gold envelope sample holder. The sample holder was then inserted in an evacuable cell, with IR transparent KBr windows, for pretreatment at 250 °C for 3 h. Afterwards, around 20 mbar of CO was dosed to the sample at RT; the cell was then closed and cooled using liquid nitrogen to favor the interaction of the probe with the samples. Once full coverage of CO on the sample surface was achieved, the probe was gradually removed through volume expansions, with the help of a vacuum line, while IR spectra were collected at each step of desorption. Once it was not possible anymore to appreciate variations in the spectral features, dynamic vacuum at 77 K was used to remove the remaining CO.

Ni K-edge XAS data were collected at the B18 beamline [28] of the Diamond Light Source (UK). XAS spectra were collected in transmission mode, using a fixed-exit double crystal water-cooled Si(111) monochromator and Pt-coated mirrors. A pair of smaller plane mirrors was used for rejection of higher harmonics. The incident (I_0) and transmitted ($I_{1,2}$) X-ray intensities were detected using ionization chambers filled with different mixtures of He and Ar (30 mbar Ar for I_0 and 230 mbar Ar for $I_{1,2}$) to result in ca. 10 % and 70 % absorption respectively. The third ionization chamber (I_2) was used for the simultaneous collection of the XANES spectrum of a Ni metal foil for the energy calibration of each spectrum [29]. Ni-functionalized MOF samples, in their as-prepared state and recovered after catalytic tests were measured at RT in air, in the form of self-supporting pellets, with optimized weights in the 80−90 mg for 1.3 cm^2 area pellets, resulting in edge jumps $\Delta\mu x$ in the 0.2–0.5 range for a total absorption after the edge of $\mu x = 2.5$. The selected model compounds (NiO, $Ni(OH)_2$, $Ni(OAc)_2(H_2O)_4$, $Ni(OAc)_2(H_2O)_2$(bpy)) were also measured in the form of self-supporting pellets, with optimized weights for transmission-mode XAS, using BN as diluent when necessary to obtain a robust enough pellet. XAS spectra were acquired in Quick-EXAFS mode in the 8133–9333 eV range (up to $k_{max} \sim 16$ $Å^{-1}$), with a constant energy step of 0.3 eV in the whole energy range. Each scan required 3 min. To characterize each pelletized sample, we collected five consecutive scans, and averaged the corresponding μx(E) curves after checking for signal reproducibility. All the XAS spectra were normalized to unity edge jump and aligned in energy using the Athena software from the Demeter package [30]. The χ(k) EXAFS functions were also extracted by using the Athena program. Fourier-transform (FT) EXAFS spectra were obtained by transforming the $k^2\chi(k)$ functions in the (2.4–14.0) $Å^{-1}$ range.

XANES linear combination fit (LCF) analysis of the spectra of (1.8)Ni-UiO-67-$bpy_{11\%}$, (3.1)Ni-UiO-67-$bpy_{11\%}$ and (1.1)Ni-UiO-67-$bpy_{6\%}$ was performed using the Athena software from the Demeter package [30], in the 8324–8384 eV energy range. The experimental XANES, μ^{EXP} (E) were fitted to a linear combination of two reference XANES spectra, μ_i^{REF} (E), *i.e.*: μ^{LCF} (E) = Σ_i w_i μ_i^{REF} (E), i = 1,2, optimizing the weights w_i for each reference spectrum. We employed as references the XANES spectra of the extremal samples in the investigated compositional series, namely (2.0) Ni-UiO-67 (representative of bpy-free Ni^{2+} species) and (0.9) Ni-UiO-67- $bpy_{11\%}$ (representative of bpy-coordinated Ni^{2+} species) LCF was performed by setting the total sum of the weights to unity, $\Sigma_i w_i = 1$. The LCF R-factor (calculated as Σ_j [$\mu^{EXP}{}_{,j}$ (E) – $\mu^{LCF}{}_{,j}$ (E)]^2/ Σ_j [$\mu^{exp}{}_{,j}$ (E,)]^2, where *j* indicates each experimental point in fitted energy range) was always $< 1 \times 10^{-4}$, indicating a very good LCF quality.

2.3. Catalytic testing

Catalytic tests were carried out in a continuous flow, fixed bed, stainless steel reactor (I.D. 8.3 mm). Before each experiment, the catalyst was pressed (0.5 tons), crushed and sieved to 240–420 μm grain size. 150–300 mg catalyst was loaded in the reactor and was activated *in situ* at 300 °C for 6 h in a flow of 10 % O_2 in He (total flow of 50 mL*min^{-1}) unless specified otherwise. The total pressure was then increased in He (up to 30 bar) and controlled by a back-pressure regulator (Bronkhorst P-702CV). During reaction, the partial pressures were controlled by adjusting individual flows. The desired mixture of ethene (3.5 grade), inert and internal standard (10 % Ne in He, 2.5 grade) was fed through the reactor, keeping the total pressure constant, but varying *e.g.* the partial pressure of ethene. Standard reaction conditions were 250 °C and 30 bar where P(ethene) =26 bar and P(inert) =4 bar and with a total flow rate of 30 mL/min (contact time at STP: 5.0 mg_{cat} min mL^{-1}_{ethene}).

A fraction of the reactor effluent, about 10 mL/min, was led through heated lines to an on-line gas chromatograph (Agilent 7890B) equipped with three columns: CP-Molsieve 5A (50 m ×0.53 mm ×50 μm) connected to TCD, GS-Gaspro (60 m ×0.32 mm) and DB-1 (40 m ×0.10 mm ×0.20 μm) both connected to FID. The three channels were used for detection of neon, light hydrocarbons up to butenes and heavier hydrocarbons, respectively. The carbon mass balance closed within ± 2 %.

3. Results and discussion

3.1. Material synthesis and characterization

Three series of catalysts with varying bpy concentration were prepared; UiO-67, UiO-67-bpy$_{6\%}$ and UiO-67-bpy$_{11\%}$ (Fig. SI 1). Ni was subsequently grafted onto the three parent materials with varying concentration. The main physical properties of the catalysts are presented in Table 1. The Ni content in the UiO-67-bpy$_{11\%}$ series varied between 0.9–3.1 wt % corresponding to Ni:bpy molar ratios from 0.5 to 1.6. Two catalysts with 0.8 and 1.1 Ni wt % were prepared for the UiO-67-bpy$_{6\%}$ series, corresponding to Ni:bpy mole ratios of 0.9 and 1.4, respectively. Ni-UiO-67, without bpy, was used as reference catalyst. Its metal concentration was determined to be 2 wt % Ni. The X-ray diffractograms of the catalysts are shown in Fig. SI 2. The XRD patterns show that all catalysts have the UiO-67 structure. No additional crystalline phase was identified, especially, the absence of diffraction peaks corresponding to NiO or Ni particles suggests that Ni is highly dispersed in the samples.

Thermogravimetric analysis (Fig. SI 3) of the three parent materials show very similar temperature stability with a decomposition temperature ~ 500 °C. Combination of solution ^{1}H-NMR and TGA measurements of the parent materials showed that their Zr node:linker ratio was between 5.1–5.4 (Table SI 1) suggesting similar defect concentration [31]. For the Ni metalated catalysts, the decomposition temperature decreased with increasing Ni concentration, independent of bpy concentration. The decomposition temperature was ~ 420 °C for the catalyst with highest concentration of Ni. In xNi-UiO-67-bpy$_{y\%}$, this difference could result from strain induced by Ni coordination to bpy linkers [32]. However, Ni might also catalyze the combustion of organic linkers, in line with the reduced stability of (2.0)Ni-UiO-67.

All parent materials had similar, high specific surface areas (S_{BET}) close to the theoretical value of 2800 m^2/g for UiO-67 [7]. Introduction of 2 wt % Ni to UiO-67 reduced the S_{BET} from ~2350 to 1540 m^2/g. Similarly, in the UiO-67-bpy$_{11\%}$ and UiO-67-bpy$_{6\%}$ series, the S_{BET} of the catalysts were found to decrease with increasing Ni loading. There were no appreciable increase in mesopore volume with increasing Ni concentration, showing that the Ni-treatment did not partially destroy the crystals to create mesopores. Prior contributions have reported that metal complexes coordinate to the bpy linker to form isolated [metal-bpy] complexes inside the MOF, and only a slight decrease in S_{BET} was reported by Gonzalez et al. [9] for (2.3)Ni-UiO-67-bpy$_{14\%}$, and by Gutterød et al. for Pt functionalized UiO-67-bpy$_{6\%}$ [13]. Molecular dynamics simulations were performed to investigate whether the loss of specific surface area with increasing Ni concentration could result from the gradual formation of a [bpy-Ni$_2$Ac$_4$] complex inside the pores, rendering the pores inaccessible for N_2 during measurement. Simulations show that the loss of specific surface area was insignificant compared to what was observed experimentally (Fig. SI 5). This result may suggest that Ni complex grafting leads to blocking of pore mouths, or to local structure distortions in the material.

Table 1
Physicochemical properties of the parent materials and Ni functionalized catalysts.

	Nickel wt. %[a]	S_{BET} (m^2/g)	V_{micro} (cm^3/g)	V_{meso} (cm^3/g)	Ni:bpy (mol/mol)
UiO-67	–	2350	0.93	0.06	–
UiO-67-bpy$_{6\%}$	–	2404	0.94	0.07	–
UiO-67-bpy$_{11\%}$	–	2431	0.97	0.06	–
(2.0)Ni-UiO-67	2.0	1540	0.62	0.10	–
(0.9)Ni-UiO-67-bpy$_{11\%}$	0.9	2146	0.83	0.07	0.5
(1.8)Ni-UiO-67-bpy$_{11\%}$	1.8	1834	0.75	0.10	1.0
(3.1)Ni-UiO-67-bpy$_{11\%}$	3.1	1549	0.68	0.10	1.8
(0.8)Ni-UiO-67-bpy$_{6\%}$	0.8	2281	0.91	0.09	0.8
(1.1)Ni-UiO-67-bpy$_{6\%}$	1.1	2156	0.88	0.09	1.5

[a] Nickel weight percent was determined by EDS analysis based on Ni/Zr ratio.

The catalysts were further analyzed with SEM to investigate the possibility of crystal degradation. SEM images of UiO-67-bpy11 %, (3.1) Ni-UiO-67-bpy$_{11\%}$, UiO-67 and (2.0)Ni-UiO-67 are shown in Fig. 2. Among the catalysts containing both bpy and Ni, crystal morphology was maintained from the parent to functionalized material. Deposition on top of the MOF crystals of (2.0)Ni-UiO-67 were observed, suggesting that the nickel acetate is either not diffusing into the pores, or diffused towards the outer surface during drying. In contrast, no deposits were observed on the surface of the highest Ni- and bpy- containing catalyst, (3.1)Ni-UiO-67-bpy$_{11\%}$ (Fig. 2B). This result suggests that bpy plays a key role in directing nickel into the pores of xNi-UiO-67-bpy$_{y\%}$, in accordance with prior literature reports [9,13]. However, for catalysts with Ni:bpy mol ratio > 1, it is evident that Ni has to form other complexes in addition to the isolated [Ni^{2+}-bpy] complex. The nature of Ni in the MOFs is further discussed in Section 3.2.

Overall, the material characterization suggests that the MOF lattice is intact after Ni functionalization, but local distortions cannot be excluded.

3.2. Catalytic testing

3.2.1. Influence of Ni and bpy concentration

The evolution of catalyst turn-over rates for ethene dimerization with time on stream under standard reaction conditions is shown in Fig. 3A. Fig. 3B and C highlight the influence of Ni:bpy ratio and bpy content in the catalysts on the ethene dimerization rate after 360 min on stream. Focusing first on Fig. 3B, UiO-67-bpy without Ni showed no conversion under the conditions used, clearly pointing to Ni as the active site. Similarly, the UiO-67-Ni catalyst without bpy linker (Ni:bpy = ∞) showed negligible conversion rate (Fig. 3 B–C), hence demonstrating the essential role of bpy linkers for grafting and activation of the Ni acetate complex.

Concentrating next on the time evolution of catalysts that contained both Ni and bpy, and focusing on the Ni-UiO-67-bpy$_{11\%}$ series, the catalysts showed an initiation period where the rate of reaction increased with TOS. This observation is consistent with a rather slow formation of the active catalyst state after the on-set of reaction. Within the Ni-UiO-67-bpy$_{11\%}$ series, the initiation period was shortest for the catalyst with high Ni content and the duration increased with decreasing Ni amount. Furthermore, the more active (3.1)Ni-UiO-67-bpy$_{11\%}$ catalyst deactivated gradually with TOS after 360 min on stream, whereas the less active catalysts had not yet reached their activity maximum after 360 or 720 min on stream (*i.e.*; the test duration), respectively. Moving next to the Ni-UiO-67-bpy$_{6\ \%}$ catalysts, it is very interesting to note that the transient behavior after on-set of reaction, as well as the turn-over rate per Ni in the catalyst at a given time on stream, were generally very similar for catalysts having the same Ni:bpy ratio, while total Ni and bpy content individually had less impact on catalyst performance (Fig. 3A–C). Fig. 3B clearly shows that the activity per Ni site increased with increasing Ni:bpy ratio, in particular for Ni:bpy ratios above 1. This result suggests that the presence of two adjacent Ni acetate complexes either facilitates the formation of the active Ni species, or creates a particularly active Ni site. It is further interesting to note that the activation and deactivation does not correlate with ethene conversion (Fig. SI 6), but with Ni:bpy mol ratio.

Turning next to product selectivity, linear butenes represented 99 % of the products in the reactor effluent, over all tested catalysts, in the studied conversion range (≤ 6 % conversion). Longer chained alkenes, denoted C_{6+}, with selectivity ~1 % were also identified. Considering the $C_4^=$ product distribution, the 1-butene : trans-2-butene : cis-2-butene ratio was 41:26:32 (Fig. SI 7). Importantly, the distribution was very similar in all catalysts, irrespective of conversion level, and far from the equilibrium distribution at the reaction temperature (see dotted lines in Fig. SI 7).

The butene isomer distribution could be primary, because of butyl

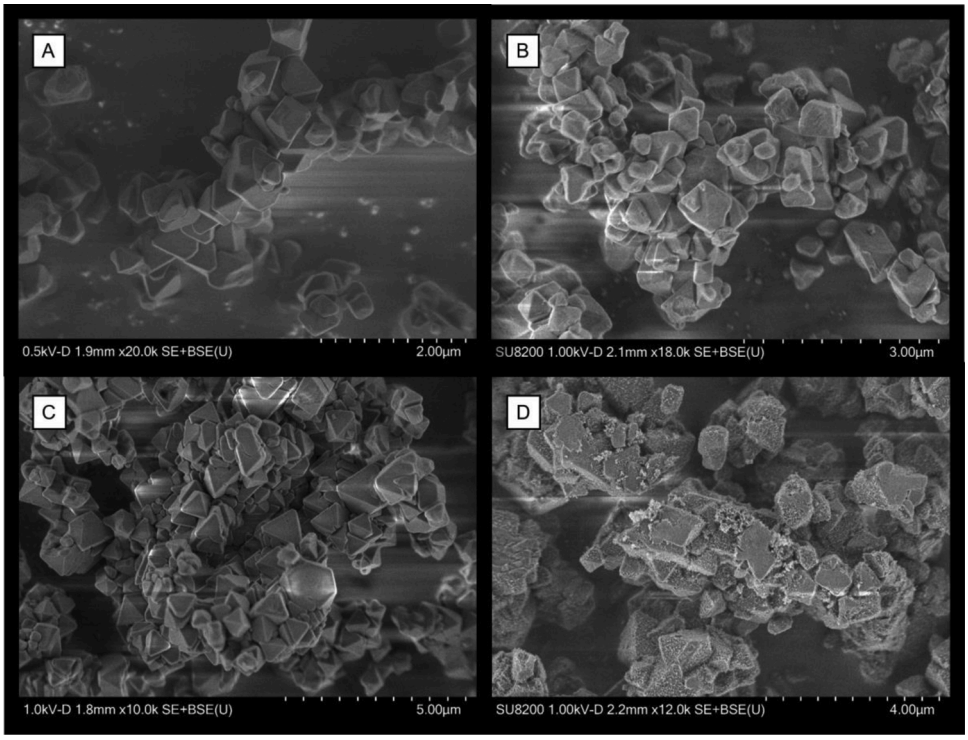

Fig. 2. SEM images of A) UiO-67-bpy$_{11\%}$, B) (3.1)Ni- UiO-67-bpy$_{11\%}$, C) UiO-67 and D) (2.0)Ni-UiO-67.

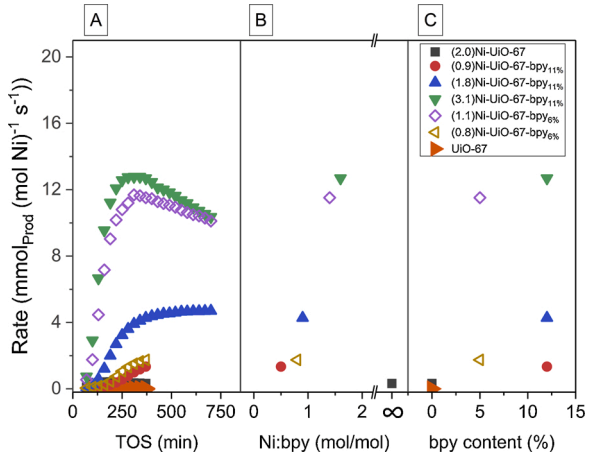

Fig. 3. A) Ethene dimerization rate vs TOS. B) Ethene dimerization rate vs Ni:bpy (mol/mol) ratio and C) vs bpy content (%) after 370 min TOS. The conversion at 370 min TOS for each catalyst shown in the legend was 0.1 %, 0.2 %, 1.1 %, 5.8 %, 1.9 %, 0.2 %, in descending order, respectively. Reaction conditions: m_{cat} =0.150 g, 30 bar total pressure where P_{ethene} =26 bar and P_{inert} =4 bar, temperature =250 °C and contact time =5.0 mg·min/mL at STP.

isomerization on the active site before desorption of the 1- or 2-butene product, or it could be secondary, due to isomerization at the Ni site or at a support site, after re-adsorption of a butene molecule. In zeolites, isomerization is mainly catalyzed by Brønsted acid sites in the zeolite lattice [23,33,34]. For this reason, we decided to investigate whether *e.g.* the μ_3-OH sites on the Zr nodes in UiO-67-bpy might catalyze the isomerization reaction, 1-butene was fed over UiO-67-bpy$_{11\%}$ at 250 °C, 1 bar total pressure. No conversion to the 2-butene isomers (or to other products) was observed (Table SI 2).

The rate of a secondary reaction is expected to depend on the concentration of the primary product. We observe that the product distribution was unaffected by change in ethene conversion, further supporting that all butenes are primary products. Together, the test data suggest that the butene isomer distribution is primary in nature, resulting from butyl isomerization on the Ni site before desorption of the butene products. The high butene selectivity and non-equilibrated butene isomer distribution point to shape selectivity as a dominant parameter in the Ni-UiO-67-bpy catalysts. Similar to what observed in Ni-SSZ-24 zeolite (Table SI 2).

These results are in accordance with the Cossee-Arlman (degenerate polymerization) mechanism, as previously suggested for other heterogeneous Ni-based ethene oligomerization catalysts [8,9,17,18]. In contrast to the metallacycle mechanism, typical of homogeneous Ni catalysts [35], the Cossee-Arlman mechanism enables isomerization of the formed butyl species before desorption from the active site. As a final note, the similar product selectivity observed for all Ni-UiO-67-bpy catalysts in this study, points to a single Ni site, positioned in a similar, well-defined, confined environment, being responsible for the activity of all catalysts. This conclusion further points to a direct correlation between the turn-over frequency of each catalyst and the fraction of Ni sites that reaches an active state after the on-set of reaction.

A comparison between the most active catalyst reported in this study, (3.1)Ni-UiO-67-bpy$_{11\%}$, and other ethene oligomerization catalysts reported in literature, shows that a higher temperature is required to achieve similar activity over Ni-UiO-67-bpy compared to silica-alumina based materials such as Ni-SSZ-24 and Ni-Beta (Table 2). Further studies are needed to establish whether the difference is due to a lower fraction of active sites, higher activation energy, or both. In either case, the disparity in reaction temperature between the two catalyst classes could arise from the difference in electron charge density on Ni as a result of varying electron donation ability of the two types of support. For homogeneous Ni catalysts, a more electrophilic metal center have been suggested to lead to an increase in the rate of ethene oligomerization, especially in the ethene insertion step (C—C coupling) [36]. Contrary to bpy ligands in UiO-67-bpy that can act as σ donors as well as π acceptors with d metals, the electron withdrawing function of zeolites may lead to a more electrophilic metal center, thus lead to an increased dimerization rate. Interestingly, both Ni-MOF and Ni-aluminosilicate

Table 2
Co-catalyst free heterogeneous catalysts for ethene dimerization in gas phase.

Catalyst	Ni (wt %)	T (°C)	P(ethene) (bar)	Conversion (%)	TOF (h^{-1})	C4 sel. (%)	Ref
Reaction in batch mode							
Ni-MFU-4l	1.0	25	50		41500	97	[10]
Ni@(Fe)-MIL-101	2.8	10	15		6300	95	[8]
Ni-MCM-48	0.5	150	35		47380	55	[38]
Ni-SBA-15	2.6	150	35		14150	54	[22]
Reaction in flow mode							
Ni-UiO-67- $bpy_{11\%}$	3.1	250	26	6	41	99	This work
Ni-SSZ-24	0.4	150	26	7	330	99	[26]
Ni-Beta	1.7	120	26	27	70	85	[34]
Ni-Beta	4.6	120	25	10	77	80	[23]
Ni-SBA-15	2.6	150	30	91	733	58	[22]

catalysts are suggested to operate through the Cossee-Arlman mechanism.

The Ni-aluminosilicate catalysts are generally operated at a rather low temperature (< 200 °C) to avoid secondary reactions such as cracking and isomerization that can take place on remaining Brønsted acid sites [23,33,34] and are active even at sub-ambient temperatures (−15 °C) [37].

The literature studies reported in Table 2 further show that testing in a continuous flow fixed-bed reactor gives significantly lower activity (TOF) compared to catalysts tested under batch conditions (Table 2). This discrepancy in activity may be a result of difference in testing conditions, evidenced by the up to 20-fold increase in activity over Ni-SBA-15 tested under similar reaction conditions when changing from flow to batch mode. Among heterogeneous Ni catalysts, Ni-MOFs are the better dimerization catalyst both in terms of activity and selectivity, but require co-catalyst in large excess.

Selectivity comparisons between the catalyst classes are complicated by the difference in reported conversion levels. However, comparing Ni-UiO-67-bpy to the 1-dimensional Ni-SSZ-24 zeolite shows very similar selectivity at similar conversion. On the other hand, the 3-dimensional Ni-Beta, that contains channel intersections that surpass the size of the Ni-SSZ-24 channels, gives substantially lower butene selectivity at comparable conversion; the main by-product being long-chain alkenes [23]. This result suggests a higher abundance of secondary reactions in those intersections, gradually blocking the pores. However, the effect of pore size is not isolated between these two materials and other properties such as acid site density and strength can play a significant role in the ethene dimerization reaction [4].

3.2.2. Catalyst stability

A major drawback of Ni-MOF catalysts associated with ethene dimerization reaction is deactivation and the complex regeneration protocol required to avoid structural damage to the framework [5]. The most common deactivation pathway reported for these catalysts is the formation of polyethylene during reaction, eventually rendering the active site inaccessible [9,11]. In the current study, deactivation over (3.1)Ni-UiO-67-$bpy_{11\%}$ with TOS was observed and this catalyst was investigated further to elucidate the deactivation pathway. Thermogravimetric analysis of the pristine and used catalyst showed that the mass of tested catalyst increased by approximately 15 % compared to the pristine catalyst, suggesting that product deposition is a reason for deactivation (Fig. 4B). In accordance with this result, the N_2 adsorption isotherm of pristine, activated and tested catalyst showed that the specific surface area of the catalyst was not notably changed after activation (Table 3). Conversely, the spent catalyst had a substantially lower specific surface area, which may best be explained by pore blocking or by MOF decomposition (Table 3).

X-ray diffractograms of pristine, activated and tested catalyst showed that the MOF catalyst was crystalline in all stages of the experiment and that the MOF framework was intact after testing (Fig. 4A). Hence, pore blocking by hydrocarbon deposits is the most probable reason for deactivation of Ni-UiO-67-$bpy_{11\%}$. Interestingly, TG-DSC analysis of pristine and tested catalyst in synthetic air revealed that prior to the framework decomposition at ~ 450 °C, the tested catalyst underwent a

Table 3
BET surface area of pristine, activated and tested catalyst determined with N_2 – adsorption. Prior to the measurement, the samples were outgassed 1 h at 80 °C and 3 h at 250 °C.

	S(BET) (m^2/g)
(3.1)Ni-UiO-67-$bpy_{11\%}$ - synthesized	1549
(3.1)Ni-UiO-67-$bpy_{11\%}$ - activated	1525
(3.1)Ni-UiO-67-$bpy_{11\%}$ - tested	503

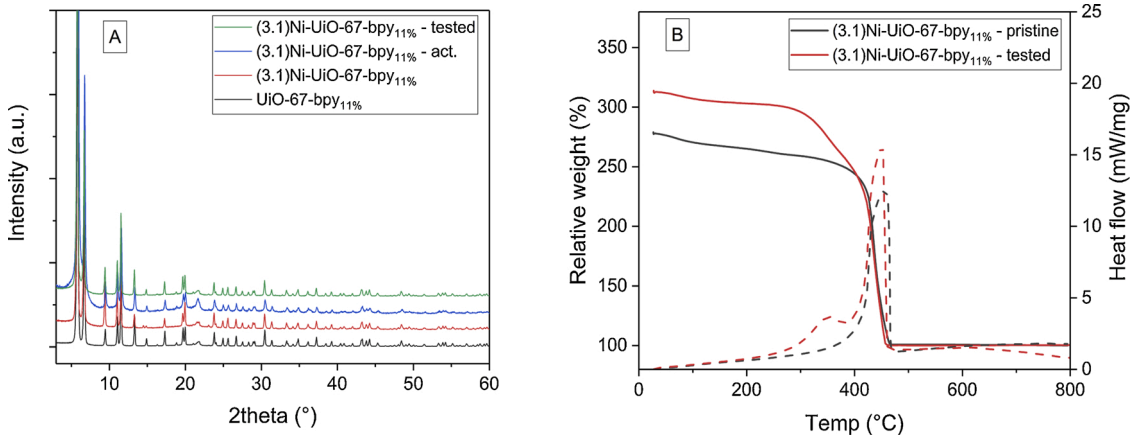

Fig. 4. A) XRD pattern of pristine, activated and tested (3.1)Ni-UiO-67-$bpy_{11\%}$. B) TG curve (solid lines) and DSC (dashed lines) of the pristine and tested (3.1)Ni-UiO-67-$bpy_{11\%}$. The samples were heated from 25 to 800 °C, 5 °C/min in a flow of synthetic air (25 mL/min).

combustion process occurring around 350 °C (Fig. 4B). The heat signal indicates that this process is exothermic, as expected from a combustion process, in contrary to what we would expect if reactions such as cracking took place during the TGA. This result indicated that the deposits are mainly lighter hydrocarbons, and that catalyst regeneration methods might be developed that enable use of the catalyst through multiple test-regeneration cycles. However, such optimization is beyond the scope of this contribution, and was not explored further.

The nature of the adsorbed products was investigated with FT-IR. Fig. 5 shows that the byproducts deposited on the porous material are predominantly linear short chain alkenes. The inset of the figure compares the residual products of reaction with the spectrum of 1-octene [39] and it is possible to observe that they possess the typical spectral features of ν_{CH2} and ν_{CH3}. Especially the presence of -CH_3 moiety let us exclude the presence of a large amount of longer oligomers of polyolefins, for whom -CH_2 is the prominent chemical species. It is difficult to completely exclude the formation of 1-octene oligomers, whose IR spectrum is very similar to the one of the monomer [40]. However, in addition to the TG and FT-IR results, XRD of the used catalyst does not show any indication either for crystalline or for amorphous polyethylene formation. Taken together with the fact that the catalysts show 99 % selectivity towards C_4 alkenes, we find long chain hydrocarbon formation very unlikely. Therefore, identification of medium chain hydrocarbons as the main carbonaceous deposit in Ni-UiO-67-bpy$_{11\%}$ further supports the strong shape selectivity of this catalyst.

3.3. FT-IR and XAS: active and spectator Ni sites

Probe molecule-assisted FT-IR is one of the simplest and most used techniques to detect and characterize active sites in heterogeneous catalysis [41]. Carbon monoxide is widely used to determine the speciation of acid sites (both Brønsted- and Lewis-type, *i.e.* acidic protons and isolated metal ions, respectively) on metal oxides, zeolites and MOFs; furthermore, it is commonly used as a probe for metal nanoparticles, due to its efficient coordination to their surfaces. All these properties make CO a perfect candidate to detect all the species that are possibly present inside our Ni-functionalized MOF catalysts. However,

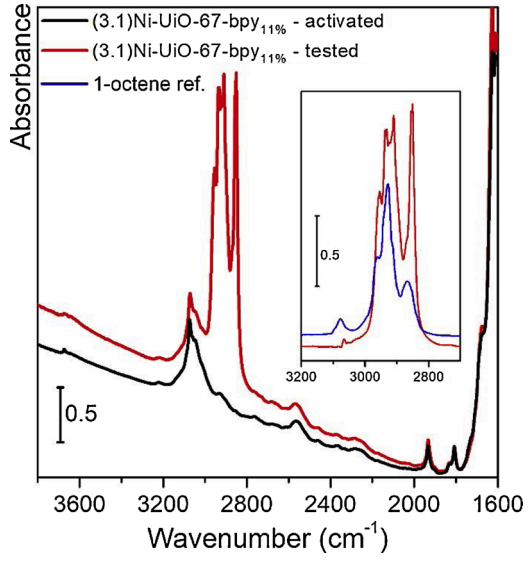

Fig. 5. FT-IR spectra of (3.1)Ni-UiO-67-bpy$_{11\%}$ sample activated for 360 min at 300 °C in 10 % O_2 (black curve), activated for 360 min and tested for 720 min (red curve). Inset shows the tested sample, after background compensation and subtraction of the only activated sample, in comparison with 1-octene FT-IR spectrum (from NIST chemistry web book [39]). (For interpretation of the references to colour in this figure legend, the reader is referred to the web version of this article).

we will begin describing the main IR features of UiO-67 (Fig. 6A). Starting from the high frequency part, we observe a tiny sharp band at 3670 cm^{-1}, related to the residual Zr-μOH at the cornerstones remaining after the thermal treatment for water removal [42,43]. ν(C-H_{arom}) stretching, belonging to the biphenyl and bipyridine linkers are arising in 3200−3000 cm^{-1} interval [42,43]. The region in which ν(C═O) from carboxylates is present (1600-1250 cm^{-1}) is excluded, since the signal is so intense as to be out of scale. In the region between 1250 and 700 cm^{-1} all the different bending modes from C-H_{arom} of the linkers are present. The most important evidence obtained from Fig. 6A is that all samples maintain the same chemical bonding typical of UiO-67 MOFs after the activation in O_2 for 360 min independently from the Ni loading present.

All samples show three evident IR bands: i) an intense band at 2135 cm^{-1}, assigned to CO physisorbed inside the material porosities [44–46]; ii) a signal at 2150 cm^{-1}, due to the interaction of CO with the residual hydroxyls terminating the Zr clusters in the MOF [46]; iii) a feature centered at 2170 cm^{-1}, ascribable to carbon monoxide interactiong with Ni^{2+} moieties [45,47,48]. The absence of bands at frequency lower than the band due to physisorbed carbon monoxide, testify the lack of metal nano-particles, for which we could expect components between 2100 and 2000 cm^{-1} [46,49–51]. We note that the intensity of the peak at 2170 cm^{-1}, assigned to CO···Ni^{2+} correlates perfectly with the total amount of Ni^{2+} moieties present in the catalysts: (*i.e.* from the one containing 3.1 wt % Ni (corresponding to Ni:bpy molar ratio of 1.6; part B) to the one having only 0.9 wt % Ni (corresponding to Ni/bpy molar ratio of 0.5; part D). Moreover we observe that Ni^{2+} is also present in the sample that does not contain bpy (part E).

We can also make the assumption that, with the given bpy concentration, we should have a good distribution of bpy across the whole MOF structure (1 linker out of 10 is a bpy, considering that UiO-67 unit cell has 6 linker molecules we have less than 1 Ni anchoring point per unit cell). Stated that, we can easily assess that Ni species are well distributed inside the MOF framework. Another variation that is possible to observe is relative to the signal at 2150 cm^{-1}; however, this can be easily correlated with slight differences in the dehydration level of Zr cornerstones of UiO-67 structure.

CO was also used to monitor the state of Ni with the specific idea to verify if Ni species had any propensity to aggregate and clustering. We decided to probe the (3.1)Ni-UiO-67-bpy$_{11\%}$ sample tested for 720 min after being activated for 360 min or 960 min, respectively, at 300 °C in 10 % O_2 (Fig. SI 8 for catalytic test and Fig. SI 9 for CO@FT-IR). Proceeding with a careful observation, it is possible to notice that the tested samples display the typical feature for CO chemisorbed on metallic Ni nanoparticles (centered at 2050 cm^{-1}), even if it has a much lower intensity than the one relative to Ni^{2+} species. A longer activation period led to a faster increase in ethene conversion, a higher conversion maximum and a more rapid deactivation. Both catalyst activated for 360 min and 960 min reached steady-state after 400 min TOS and the conversion and deactivation rates over both catalysts converged. At this point, the catalysts are hypothesized to be in similar state *i.e.* same relative concentration of the active nickel species. The curves corresponding to tested (3.1)Ni-UiO-67-bpy$_{11\%}$ samples activated for 360 min (violet) or 960 min (green) perfectly overlap along the whole spectral region, displaying an identical amount of Ni^{2+} able to chemisorb CO. The only appreciable difference, highlighted in the inset of Fig. SI 9, concerns the amount of Ni nanoparticles present in the sample.

The spectrum of the sample only activated for 360 min did not display any sign of Ni or NiO nanoparticles, eliminating the possibility of nanoparticle formation during the activation process. Considering that nanoparticles were not observed on the other catalysts, Ni and NiO nanoparticles can be ruled out as the active site, leaving Ni^{2+} as the most likely active site for ethene dimerization. Furthermore, nickel aggregation to form nanoparticles suggests that nickel is mobile and may be a secondary deactivation path.

Ni K-edge XAS provided complementary information on the average Ni-speciation and local coordination environment in Ni-functionalized

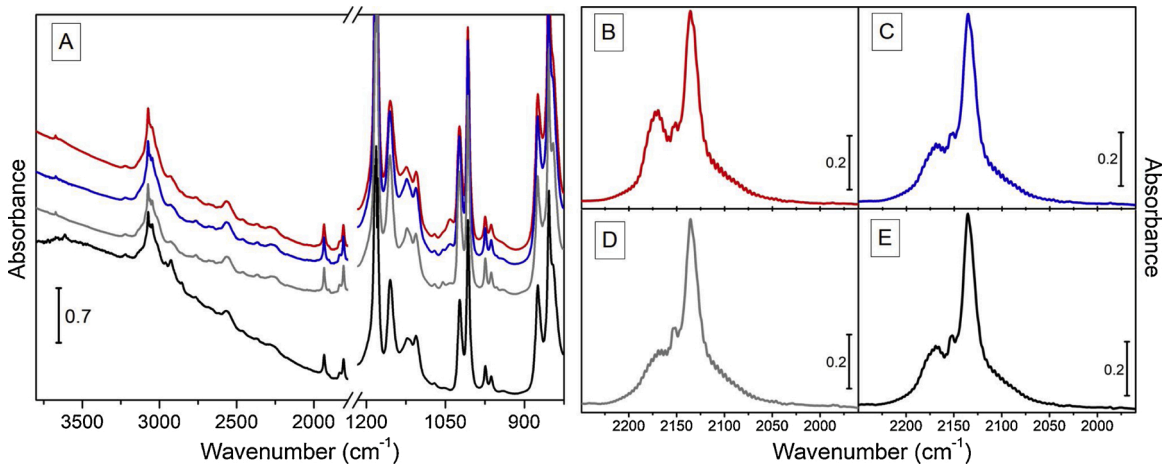

Fig. 6. A) FT-IR spectra of UiO-67-bpy$_{11\%}$ samples with different Ni(OAc)$_2$ content (3.1 wt % - red curve; 1.8 wt % - blue curve; 0.9 wt % - grey curve) and of (2.0)Ni-UiO-67 (black curve) after activation for 360 min at 300 °C in 10 % O_2. The carboxylates spectral region (1700-1250 cm^{-1}) is excluded since it is out of scale. CO@77 K FT-IR spectra of UiO-67-bpy$_{11\%}$ samples with different Ni(OAc)$_2$ content (3.1 wt % - part B; 1.8 wt % - part C; 0.9 wt % - part D) and of (2.0)Ni-UiO-67 (part E). All the plotted spectra in parts B-C-D-E represent the maximum coverage of CO (θ_{MAX}) after the subtraction of the spectra at minimum coverage (θ_{min}). The spectra are then normalized with respect to the peak at 2135 cm^{-1} (physisorbed CO), which takes into account not only the total amount of CO that is dosed but also the pellet thickness. (For interpretation of the references to colour in this figure legend, the reader is referred to the web version of this article).

MOF catalysts, in their as-prepared state as well as after activation and reaction.

These evidences can be rationalized in line with the compositional characteristics of the two extremal samples. Indeed, (2.0) Ni-UiO-67 is representative of Ni^{2+} ions incorporated in the UiO-67 MOF environment in the absence of privileged anchoring points at bpy-linkers. The intense WL in its XANES spectra closely resemble what is observed in the Ni(OAc)$_2$(H$_2$O)$_4$ precursor. Nonetheless, we note a slight shift to higher energy of the WL peak in the XANES of (2.0) Ni-UiO-67 with respect to what is observed in the model compound, together with certain differences in the 2−4 Å range in FT-EXAFS. Such deviations suggest that the MOF could play an active role – although to a minor extent in the absence of bpy - in directing the incorporation of Ni-species from the Ni(OAc)$_2$(H$_2$O)$_4$ precursor. Ni(OAc)$_2$(H$_2$O)$_4$ deposits at the outer crystal surfaces, observed by SEM for (2.0) Ni-UiO-67, could coexist with different Ni^{2+} moieties inside the MOFs scaffold, possibly interacting with defects at the UiO-67 nodes.

Conversely, (0.9) Ni-UiO-67- bpy$_{11\%}$, with Ni:bpy (mol/mol) = 1:2, provides a large excess of bpy linkers with respect to Ni ions, resulting in almost exclusive presence of bpy-coordinated Ni^{2+} moieties inside the MOF scaffold: comparing the (0.9) Ni-UiO-67- bpy$_{11\%}$ XAS data with the ones obtained for a series of well-characterized bpy-OAc Ni^{2+} complexes, we found the best agreement in both the XANES and EXAFS region with a Ni(OAc)$_2$(H$_2$O)$_2$(bpy) model complex, structurally characterized by single crystal XRD (see Fig. SI 10).

We were able to properly model the XANES of the remaining three catalysts, namely (1.8)Ni-UiO-67-bpy11 %, (3.1)Ni-UiO-67-bpy$_{11\%}$ and (1.1)Ni-UiO-67-bpy$_{6\%}$, as linear combinations of the spectra collected for the two extremal materials. Linear combination fit (LCF) analysis resulted in R-factors lower than 1×10^{-4}, corroborating the validity of the adopted model. As illustrated by the pie charts in Fig. 7A, an increased Ni:bpy ratio translates in the progressive increase of bpy-free

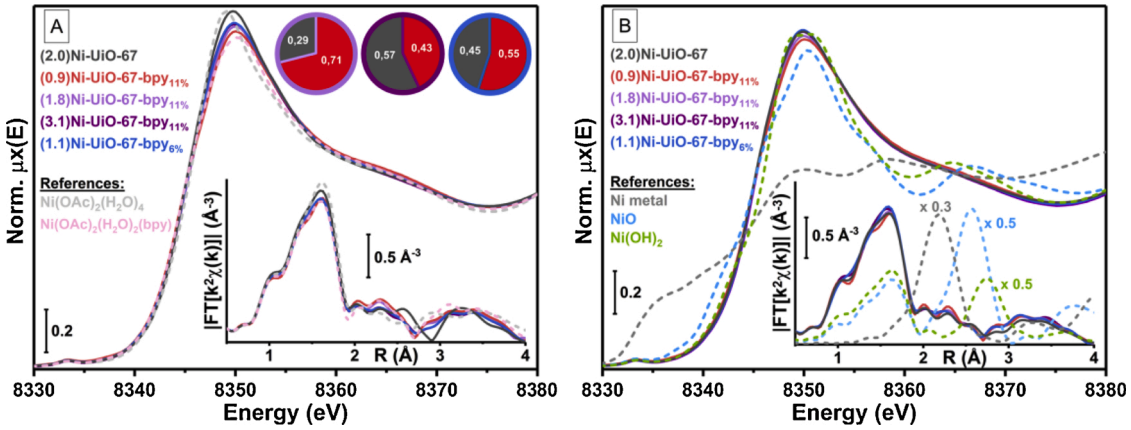

Fig. 7. (A) Ni K-edge XANES of as-prepared Ni-functionalized MOF catalysts. The bottom inset shows the corresponding phase-uncorrected FT-EXAFS spectra, obtained transforming the k^2-weighted k$^2\chi$(k) curves in the 2.4-14.0 Å^{-1} range. Pie charts illustrate Ni-speciation in samples (1.8)Ni-UiO-67-bpy$_{11\%}$ (light purple), (3.1)Ni-UiO-67-bpy$_{11\%}$ (purple) and (1.1)Ni-UiO-67-bpy$_{6\%}$ (blue) estimated from XANES LCF analysis using as references the spectra of the (2.0) Ni-UiO-67 (grey) and (0.9) Ni-UiO-67- $_{bpy11\%}$ (red), representative of Ni^{2+} species incorporated into bpy-free UiO-67 and Ni^{2+} species coordinated to bpy linkers in UiO-67-bpy MOFs, respectively. LCF errors on reported Ni fractions are of ± 0.02 in all cases. XANES and FT-EXAFS spectra of relevant model compounds are also reported as dashed lines, including Ni(OAc)$_2$(H$_2$O)$_4$ (light grey) and Ni(OAc)$_2$(H$_2$O)$_2$(bpy) (pink). (B) As part (A) but for Ni-functionalized MOF catalysts recovered after catalytic tests. XANES and FT-EXAFS spectra of bulk Ni metal (grey), NiO (light blue) and Ni(OH)$_2$ (green) are also reported as dashed lines, scaled by appropriate factors in the FT-EXAFS for an easier comparison with the spectra of the Ni-functionalized MOF catalysts. (For interpretation of the references to colour in this figure legend, the reader is referred to the web version of this article).

Ni^{2+} moieties at the expenses of bpy-coordinated Ni^{2+} species. Interestingly, we observe a very similar fractional distribution among bpy-free and bpy-coordinated Ni^{2+} species in as-prepared (3.1)Ni-UiO-67-$bpy_{11\%}$ and (1.1)Ni-UiO-67-$bpy_{6\ \%}$, close in both cases to 50 % total Ni for each component: this falls in line with the equivalent rates observed for the ethene dimerization reaction over the two catalysts (Fig. 3).

From Fig. 7A it is also clear that no large metallic or oxidic aggregates are detectable in the as-prepared catalysts: in agreement with the CO FT-IR and PXRD results, Ni-speciation is dominated by well-dispersed Ni^{2+} species. Most importantly, the same conclusion can be reached after activation and reaction. With this respect, Fig. 7B reports a direct comparison between the XAS spectra of Ni-functionalized MOFs recovered after catalytic tests and of Ni metal, NiO and $Ni(OH)_2$ model compounds.

The XANES line shape remains similar to the one observed in the as-prepared materials, diagnostic for (pseudo)-octahedral Ni^{2+} species. However, we note a global broadening and dampening in the WL, accompanied with a general reduction of the differences discussed above between the different catalysts in the series, in both the XANES and EXAFS regions. Albeit subtle, such modifications with respect to the as-prepared materials underpin reorganization of Ni-species during activation and catalysis, likely involving interaction between the dehydrated form of bpy-coordinated and bpy-free Ni^{2+}-species discussed before. These phenomena will be addressed in more detail in future, with dedicated XAS studies carried out under *in situ* and *operando* conditions.

Exposure to the atmosphere after testing is expected to result into a prompt coordination of H_2O molecules to exposed Ni sites generated after activation, thus restoring an octahedral environment around the metal centers. Nonetheless, if metal or oxide/hydroxide phases would have formed under activation and/or reaction conditions, these should be detectable by XAS at the adopted experimental conditions. In this respect, no traces of the characteristic fingerprints of Ni metal, NiO or Ni$(OH)_2$ are observed in the XANES. In parallel, in the EXAFS, well-defined scattering features in the 2−3 Å range (phase uncorrected), characteristic of Ni-Ni contributions in the considered aggregate phases, are absent, within the detection limits of the technique (typically, 5 % total Ni). In substantial agreement with FT-IR results, XAS points to dispersed Ni^{2+} species as the active sites for the ethene dimerization reaction. These could include Ni-monomers or, plausibly, low-nuclearity Ni-multimers, docked at bpy linkers with Ni-Ni distances > 4 Å, eluding an efficient detection by EXAFS.

4. Conclusion

The results obtained in this study confirm the potential of co-catalyst free Ni-UiO-67-bpy as ethene dimerization catalysts. Spectroscopic investigations point to well-distributed Ni^{2+} sites, probably in the form of low-nuclearity Ni-multimers docked at bpy linkers, as the main active site for the ethene dimerization reaction. Those sites, and the surrounding UiO-67 lattice, impose strong shape selectivity on the reacting species, leading to exceptionally high selectivity (99 %) to linear 1- and 2-butenes in the gas phase, and to medium chain hydrocarbons as the dominant deposits in the catalyst after deactivation. Notably, all linear butenes were primary in nature and the selectivity was controlled by kinetic factors, providing an opportunity to tune the selectivity of the reaction towards the α-olefin, 1-butene. The high versatility of MOFs in terms of both their extraordinary degree of variability and the potential control over the active site opens up the possibility for tailored MOF ethene dimerization catalysts in the future.

CRediT authorship contribution statement

Mustafa Kømurcu: Conceptualization, Investigation, Formal analysis, Writing - original draft, Writing - review & editing. **Andrea Lazzarini:** Investigation, Formal analysis, Writing - original draft, Writing - review & editing. **Gurpreet Kaur:** Investigation, Formal analysis, Writing - original draft. **Elisa Borfecchia:** Investigation, Formal analysis, Writing - original draft. **Sigurd Øien-Ødegaard:** Investigation, Formal analysis. **Diego Gianolio:** Investigation, Formal analysis. **Silvia Bordiga:** Formal analysis, Writing - original draft, Supervision. **Karl Petter Lillerud:** Supervision. **Unni Olsbye:** Conceptualization, Data curation, Writing - original draft, Writing - review & editing, Supervision, Project administration.

Declaration of Competing Interest

The authors declare that they have no known competing financial interests or personal relationships that could have appeared to influence the work reported in this paper.

Acknowledgements

The Research Council of Norway is acknowledged for financial support of this work through project no. 250795 (CONFINE). We acknowledge Diamond Light Source for time on Beamline B18 under Proposal SP21713-1.

Appendix A. Supplementary data

Supplementary material related to this article can be found, in the online version, at doi:https://doi.org/10.1016/j.cattod.2020.03.038.

References

[1] J.N. Armor, Key questions, approaches, and challenges to energy today, Catal. Today 236 (Part B) (2014) 171–181.
[2] P.-A.R. Breuil, L. Magna, H. Olivier-Bourbigou, Role of homogeneous catalysis in oligomerization of olefins : focus on selected examples based on group 4 to group 10 transition metal complexes, Catal. Letters 145 (1) (2014) 173–192.
[3] D.S. McGuinness, Olefin oligomerization via Metallacycles: dimerization, trimerization, tetramerization, and beyond, Chem. Rev. 111 (3) (2010) 2321–2341.
[4] A. Finiels, F. Fajula, V. Hulea, Nickel-based solid catalysts for ethylene oligomerization - a review, Catal. Sci. Technol. 4 (8) (2014) 2412–2426.
[5] V. Hulea, Toward platform chemicals from bio-based ethylene: heterogeneous catalysts and processes, ACS Catal. 8 (4) (2018) 3263–3279.
[6] J.H. Cavka, et al., A new zirconium inorganic building brick forming metal organic frameworks with exceptional stability, J. Am. Chem. Soc. 130 (42) (2008) 13850–13851.
[7] S. Øien-Ødegaard, et al., UiO-67-type metal–organic frameworks with enhanced water stability and methane adsorption capacity, Inorg. Chem. 55 (5) (2016) 1986–1991.
[8] J. Canivet, et al., MOF-supported selective ethylene dimerization single-site catalysts through one-pot postsynthetic modification, J. Am. Chem. Soc. 135 (11) (2013) 4195–4198.
[9] M. Gonzalez, J. Oktawiec, J.R. Long, Ethylene Oligomerization in Metal-Organic Frameworks Bearing Nickel(II) 2,2[prime or minute]-Bipyridine Complexes, Faraday Discussions, 2017.
[10] E.D. Metzger, et al., Selective dimerization of ethylene to 1-butene with a porous catalyst, ACS Cent. Sci. 2 (3) (2016) 148–153.
[11] S.T. Madrahimov, et al., Gas-phase dimerization of ethylene under mild conditions catalyzed by MOF materials containing (bpy)NiII complexes, ACS Catal. 5 (11) (2015) 6713–6718.
[12] Z. Li, et al., Sintering-resistant single-site nickel catalyst supported by metal–organic framework, J. Am. Chem. Soc. 138 (6) (2016) 1977–1982.
[13] E.S. Gutterød, et al., CO2 hydrogenation over Pt-containing UiO-67 Zr-MOFs—the base case, Ind. Eng. Chem. Res. 56 (45) (2017) 13206–13218.
[14] B. Liu, et al., Postsynthetic modification of mixed-linker metal–organic frameworks for ethylene oligomerization, RSC Adv. 4 (107) (2014) 62343–62346.
[15] S. Yuan, et al., Exposed equatorial positions of metal centers via sequential ligand elimination and installation in MOFs, J. Am. Chem. Soc. 140 (34) (2018) 10814–10819.
[16] A.N. Mlinar, et al., Selective propene oligomerization with nickel(II)-Based metal–organic frameworks, ACS Catal. 4 (3) (2014) 717–721.
[17] E.D. Metzger, et al., Mechanism of single-site molecule-like catalytic ethylene dimerization in Ni-MFU-4l, J. Am. Chem. Soc. 139 (2) (2017) 757–762.
[18] V. Bernales, et al., Computationally guided discovery of a catalytic cobalt-decorated metal–organic framework for ethylene dimerization, J. Phys. Chem. C 120 (41) (2016) 23576–23583.
[19] E.J. Arlman, P. Cossee, Ziegler-Natta catalysis III. Stereospecific polymerization of propene with the catalyst system TiCl3 AlEt3, J. Catal. 3 (1) (1964) 99–104.

[20] R.Y. Brogaard, U. Olsbye, Ethene oligomerization in Ni-containing zeolites: theoretical discrimination of reaction mechanisms, ACS Catal. (2016) 1205–1214.
[21] K. Toch, J.W. Thybaut, G.B. Marin, Ethene oligomerization on Ni-SiO2-Al2O3: experimental investigation and single-event MicroKinetic modeling, Appl. Catal. A Gen. 489 (2015) 292–304.
[22] R.D. Andrei, et al., Heterogeneous oligomerization of ethylene over highly active and stable Ni-AlSBA-15 mesoporous catalysts, J. Catal. 323 (2015) 76–84.
[23] R. Henry, et al., Ethene oligomerization on nickel microporous and mesoporous-supported catalysts: investigation of the active sites, Catal. Today 299 (2018) 154–163.
[24] A. Ehrmaier, et al., Dimerization of linear Butenes on zeolite-supported Ni2+, ACS Catal. 9 (1) (2019) 315–324.
[25] R. Joshi, et al., Evidence for the coordination–insertion mechanism of ethene dimerization at nickel cations exchanged onto Beta molecular sieves, ACS Catal. 8 (12) (2018) 11407–11422.
[26] R.Y. Brogaard, et al., Ethene dimerization on zeolite-hosted Ni ions: reversible mobilization of the active site, ACS Catal. 9 (6) (2019) 5645–5650.
[27] S. Øien-Ødegaard, Preparation, structure and reactivity of functionalized zirconium metal-organic frameworks, Oslo (2016).
[28] A.J. Dent, et al., B18: a core XAS spectroscopy beamline for diamond, J. Phys. Conf. Ser. 190 (2009) 012039.
[29] S. Bordiga, et al., Reactivity of surface species in heterogeneous catalysts probed by in situ X-ray absorption techniques, Chem. Rev. 113 (3) (2013) 1736–1850.
[30] B. Ravel, M. Newville, ATHENA, ARTEMIS, HEPHAESTUS: data analysis for X-ray absorption spectroscopy using IFEFFIT, J. Synchrotron Radiat. 12 (4) (2005) 537–541.
[31] G. Kaur, et al., Controlling the synthesis of metal–organic framework UiO-67 by tuning its kinetic driving force, Cryst. Growth Des. 19 (8) (2019) 4246–4251.
[32] M.I. Gonzalez, et al., Single-crystal-to-single-crystal metalation of a metal–organic framework: a route toward structurally well-defined catalysts, Inorg. Chem. 54 (6) (2015) 2995–3005.
[33] M. Sanati, C. Hornell, S.G. Jaras, The oligomerization of alkenes by heterogeneous catalysts, in: Catalysis, vol. 14, The Royal Society of Chemistry, 1999, pp. 236–288.
[34] A. Martínez, et al., New bifunctional Ni–H-beta catalysts for the heterogeneous oligomerization of ethylene, Appl. Catal. A Gen. 467 (2013) 509–518.
[35] F. Speiser, P. Braunstein, L. Saussine, Catalytic ethylene dimerization and oligomerization: recent developments with nickel complexes containing P,N-chelating ligands, Acc. Chem. Res. 38 (10) (2005) 784–793.
[36] S.A. Svejda, M. Brookhart, Ethylene oligomerization and propylene dimerization using cationic (α-Diimine)nickel(II) catalysts, Organometallics 18 (1) (1999) 65–74.
[37] I. Agirrezabal-Telleria, E. Iglesia, Stabilization of active, selective, and regenerable Ni-based dimerization catalysts by condensation of ethene withinordered mesopores, J. Catal. 352 (2017) 505–514.
[38] M. Lallemand, et al., in: R. Xu (Ed.), Ethylene Oligomerization Over Ni-Containing Mesostructured Catalysts With MCM-41, MCM-48 and SBA-15 Topologies, in Studies in Surface Science and Catalysis, Elsevier, 2007, pp. 1863–1869.
[39] O. Atkins, Weller Rourke, Armstrong, Inorganic Chemistry, OUP Oxford, 2009.
[40] T.C. Chung, Functionalized polyolefins via copolymerization of borane monomers in Ziegler-Natta process, in: J.C. Salamone, J.S. Riffle (Eds.), Advances in New Materials, Springer US, Boston, MA, 1992, pp. 323–331.
[41] C. Lamberti, et al., Probing the surfaces of heterogeneous catalysts by in situ IR spectroscopy, Chem. Soc. Rev. 39 (12) (2010) 4951–5001.
[42] S. Chavan, et al., H2storage in isostructural UiO-67 and UiO-66 MOFs, J. Chem. Soc. Faraday Trans. 14 (5) (2012) 1614–1626.
[43] M. Kandiah, et al., Post-synthetic modification of the metal–organic framework compound UiO-66, J. Mater. Chem. 20 (44) (2010) 9848–9851.
[44] S. Bordiga, et al., Low temperature CO adsorption on Na-ZSM-5 zeolites: an FTIR investigation, J. Catal. 137 (1) (1992) 179–185.
[45] S. Chavan, et al., Response of CPO-27-Ni towards CO, N_2 and C_2H_4, J. Chem. Soc. Faraday Trans. 11 (42) (2009) 9811–9822.
[46] V.A. Sadykov, et al., Ni-loaded nanocrystalline ceria-zirconia solid solutions prepared via modified Pechini route as stable to coking catalysts of CH_4 dry reforming, Open Chem. 14 (1) (2016) 363–376.
[47] E.D. Bloch, et al., Reversible CO binding enables tunable CO/H_2 and CO/N_2 separations in metal-organic frameworks with exposed divalent metal cations, J. Am. Chem. Soc. 136 (30) (2014) 10752–10761.
[48] S. Chavan, et al., CO adsorption on CPO-27-Ni coordination polymer: spectroscopic features and interaction energy, J. Phys. Chem. C 113 (8) (2009) 3292–3299.
[49] C. Hu, et al., Temperature-programmed FT-IR study of the adsorption of CO and co-adsorption of CO and H_2 on $NiAl_2O_3$, J. Mol. Catal. A Chem. 110 (2) (1996) 163–169.
[50] J.B. Peri, Infrared studies of Ni held at low concentrations on alumina supports, J. Catal. 86 (1) (1984) 84–94.
[51] S. Tada, et al., N_2O pulse titration of Ni/α-Al_2O_3 catalysts: a new technique applicable to nickel surface-area determination of nickel-based catalysts, J. Phys. Chem. C 117 (28) (2013) 14652–14658.